Surface Characterization and Optimization of Porous Zinc Anodes to Improve Cycle Stability by Mitigating Dendritic Growth

Journal of The Electrochemical Society, 2022 **169** 100511
1945-7111/2022/169(10)/100511/7/$40.00 © 2022 The Electrochemical Society ("ECS"). Published on behalf of ECS by IOP Publishing Limited

Surface Characterization and Optimization of Porous Zinc Anodes to Improve Cycle Stability by Mitigating Dendritic Growth

Matthew Powell and Shuya Wei[*,z]

Department of Chemical and Biological Engineering, University of New Mexico, Albuquerque, New Mexico, United States of America

Zinc-based batteries are a scalable and safe alternative to Lithium-ion batteries due to the nature of abundance, low cost and easy to process. In this work, we have successfully synthesized porous zinc electrodes (PZEs) via a gel-binder method that can stably charge and discharge for over 700 h at 1 mA cm^{-2} before showing signs of failure. We compared PZEs synthesized from small (60 nm), intermediate (10 μm), and large (150 μm) zinc particles to determine which surface features are best suited to mitigate dendritic growth and to improve electrolyte stability. The zinc deposits on the large PZE shows a stable and flat morphology, which does not form the hexagonal close-packed (HCP) crystal structure that is typically seen on planar zinc anodes. The intermediate PZE has an increased affinity to deposit onto the glass microfiber separator leading to a decrease of active material on the anode that causes instability during galvanostatic cycling. Both planar zinc and small PZE show HCP deposits that are normal to the surface, which result in very poor electrochemical performance. As the particle size increases, the deposits transition from HCP crystals to flat amorphous metal deposits, increasing cyclic stability.
 [DOI: 10.1149/1945-7111/ac9649]

Manuscript submitted June 7, 2022; revised manuscript received August 11, 2022. Published October 10, 2022.

Supplementary material for this article is available online

The current energy storage market has been dominated by Lithium-ion batteries (LiBs) during the twenty-first century.[1,2] However, LiBs are reaching their theoretical limit, so researchers are now looking into alternative battery chemistries that have higher theoretical energy densities and larger capacities.[3] One potential solution is to fabricate metal anode batteries. Metal anodes provide a much larger theoretical capacity than metal ion batteries, however, several fundamental challenges still need to be overcome before metal anode batteries are able to compete and replace LiBs in the global energy storage market as well as being used for grid storage application.[4] Additionally, lithium-based batteries require lithium and other expensive rare earth metals such as cobalt that require extensive extraction techniques. Furthermore, lithium is dangerous to work with and can react with air, so an inert atmosphere is required to process and assembly lithium-based batteries.[5,6] One potential alternative to LiBs is zinc-based batteries. Zinc is an abundant and inexpensive metal that is found all around the globe. It is safe to work with, nonreactive in air, and can work in aqueous conditions.[7–9] However, like all other metal-anode batteries, zinc anodes are prone to the same failure mechanisms. Metal anodes in aqueous electrolytes typically fail from one of the following mechanisms: (1) passivation layer formation; (2) dendrite formation; (3) hydrogen evolution; and (4) other undesired side reactions.[10–13] These failure mechanisms can be visualized in Fig. 1A.

Researchers have tried a variety of potential solutions to improve the plating mechanics of the zinc metal anode. They found that the cycle life of the cell can be improved through electrolyte optimization,[9,14,15] the addition of alloys to the metal,[16] metal coating[17–19] and using a porous 3-D structure in place of the standard 2D planar structure.[20] It has been found that using a porous structure as the anode in place of planar metal can suppress dendrite growth by increasing the effective diffusion limiting current, weakening the local electric field strength. It allows for even plating cycles and prevents the dendritic growth on the anode.[21] As shown in Fig. 1B, we propose a schematic diagram showing theoretical plating patterns on porous zinc electrodes (PZEs).

Herein we report a binder fabrication method using different starting zinc particle sizes to determine optimal surface area, porosity, zinc-to-zinc oxide ratio to maximize cycle stability and mitigate dendrite growth. From our findings, we are able to report a porous zinc anode made from large (150 μm) starting particles that are stable for 700 h without showing signs of failure. The large PZE also exhibits an increase in electrolyte stability, showing an increase of 300 h of plating and stripping before the electrolyte begins to degrade when compared to planar zinc. The bulk and interfacial resistance of the cell is also decreased when switching from the planar zinc to the porous zinc, resulting in a lower over potential to be required to strip and plate the zinc ions. These batteries utilize 2 M $ZnSO_4$ + 5% PEG 300 as it a common electrolyte used in zinc batteries[22] and PEG additives have been shown to increase the performance of zinc batteries.[23,24]

Materials & Methods

All materials were bought commercially and were not modified in any manner. 150 μm zinc (99%) was obtained from Goodfellow. 10 μm zinc (99%) was obtained from Sigma Aldrich. 60 nm zinc (99%) was obtained from Sigma Aldrich. 0.1 mm thick planar zinc (99.9%) was obtained from MTI. Zinc sulfate anhydride (99.5%) was obtained from Sigma Aldrich. All coin cell parts were CR2032-C-304SS. 934-Ah glass microfiber separators were obtained from Cytiva. Polyethylene glycol 300 (PEG300) was obtained from Sigma Aldrich. Zinc oxide (99.9%) was obtained from Sigma Aldrich. Polytetrafluoroethylene (PTFE) was obtained from Sigma Aldrich. Sodium dodecylbenzenesulfonate (SDBS, technical grade) was obtained from Sigma Aldrich.

Anode Fabrication

The fabrication method used to make PZEs was modified from a previous publication from Sandia National Laboratories.[25] To make the anode, 83 wt% zinc, 9.8 wt% zinc oxide, 2.2 wt% SDBS, and 5 wt% PTFE were combined in a mortar and pestle and were thoroughly mixed to form a puddy by adding small amounts of isopropyl alcohol (IPA) as needed for 1 h. Next, the puddy was roller pressed until the puddy was flat and around 1 mm in thickness. The puddy was then cut into circles with ½ inch or 5/8-inch diameters as the PZE electrodes. The PZEs were then put in the vacuum oven to be dried over night at a temperature of 60 °C and at a pressure of 650 mmHg. The dried PZEs were assembled into coin cells. PZEs were made using small (60 nm), intermediate (10 μm), and large (150 μm) starting zinc particle sizes. The ½ inch intermediate PZE had an average of 0.19113 g of active material and the large PZE of the same diameter had an average of 0.20775 g of active material. The ½ inch planar zinc weigh an average of 0.10 g. Coin cell parts

*Electrochemical Society Member.
[z]E-mail: swei@unm.edu

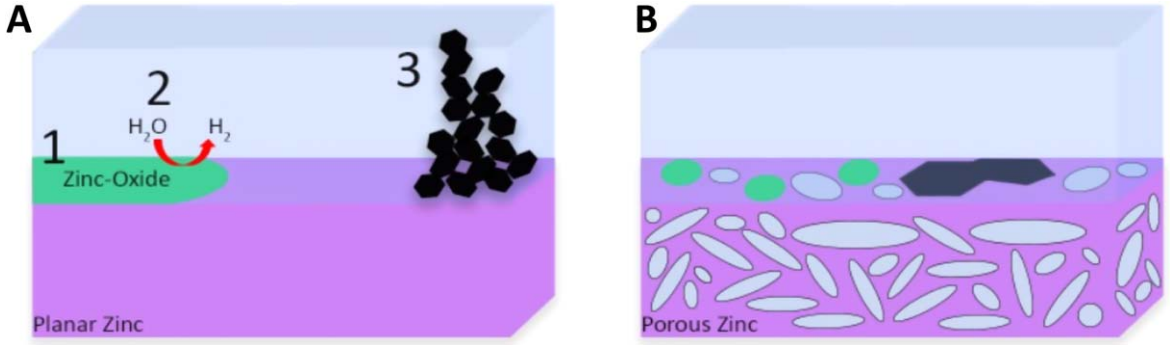

Figure 1. Schematic diagram of plating patterns on a planar zinc and a porous zinc electrode, as well as failure mechanisms that plague metal anodes. (a) Planar zinc and several failure mechanisms including: (1) an insulating layer of zinc oxide that passivates on the surface of the anode; (2) hydrogen evolution producing hydrogen gas and degrading the electrolyte and (3) dendrite formation, uneven plating causing tree like branches to form over repeated cycles until the separator is pieced and a bridge between the electrodes is formed causing the cell to short. (b) proposed dendrite plating structure on a porous zinc anode.

were washed in acetone and DI water prior to assembly. Symmetric Zn||Zn coin cells were assembled by placing the larger PZE electrode into the bottom cap followed by the separator. 100 μL of 2 M $ZnSO_4$ with 5 wt% PEG300 electrolyte was then added to the separator. The smaller PZE electrode was placed on top followed by the spacer and wave spring. The top cap was then placed on the top, and the cell was sealed using a battery crimper. Planar symmetric Zn||Zn cells were made in a similar method using planar zinc that was cut into the same sizes as the PZEs. Zinc vs stainless steel cells were made by using a 304 SS disk in place of the larger PZE. Visualization of cell assembly can be found in Supporting information Fig. 1. Celgard 3401 and Celgard 2500 were also considered but not used as they did not adsorb the electrolyte.

Electrochemical Characterization

Electrochemical impedance spectroscopy (EIS) and linear sweep voltammetry (LSV) were performed using a Biologic electrochemical potentiostat. EIS was conducted using a 5 mV AC amplitude from open circuit potential in a frequency range from 200 kHz to 100mHz. LSV was conducted using a scan rate of 1 mVs^{-1} in a range of −0.2 V to 5 V vs the reference electrode of zinc. Depth of discharge (DoD_{zn}) and galvanostatic stripping tests were performed using a Neware mass battery tester. Galvanostatic constant current tests were conducted using currents ranging from 1 m Acm^{-2} to 5 $mAcm^{-2}$. Batteries were discharged and charged for one hour at a time with a minute rest in between for ten, twenty, one hundred cycles, or until failure using the various currents. DoD_{zn} tests were conducted by discharging zinc vs stainless steel electrode under a constant current of 1 $mAcm^{-2}$. Anodes were pre-weighed before assembly to determine the amount of active material inside of the PZEs.

Material Characterization of Electrodes

Pristine anodes were fabricated and characterized before placing into a cell. Cycled cells were opened, where anodes were washed with the $ZnSO_4$ electrolyte and then methanol to remove any residual electrolyte and separator pieces. The washed electrodes were then dried at 60 °C overnight in a vacuum oven at 600 mmHg. Scanning electron microscopy (SEM) was performed using a Tescan Vega 3 and energy dispersive spectroscopy (EDS) was performed using an IXRF Iridium Ultra with an SSD X-ray detector with an accelerator voltage of 20 kV at a working distance ranging from 0.17 mm to 0.22 mm. XRD was performed using a Rigaku SmartLab X-ray diffractometer. Brunauer–Emmett–Teller (BET) surface area analysis was performed using a Micromeritics Gemini 2360 Surface Area Analyzer using liquid nitrogen as the coolant.

Results and Discussion

Porous zinc anodes were fabricated and characterized under SEM to compare the surface morphology of the electrodes made from different starting zinc particle sizes. Visualization of the surfaces of the electrodes are used to determine the optimal morphology, porosity, and zinc-to-zinc oxide surface ratio. The electrode surfaces are characterized at both pristine state and at different stages of galvanostatic cycling conditions to study the morphology evolution under cycling conditions. The porosity and the surface area of the PZEs need to be confirmed at first before preforming any electrochemical characterization tests. BET analysis was done to confirm that the PZEs are porous and to determine their surface areas (Supporting information Fig. 2). The surface area of the large PZE is found to be 2.23 m^2g^{-1}, while the intermediate PZE has a larger surface area of 3.0 m^2g^{-1}. The small PZE has the largest surface area of the three at 3.04 m^2g^{-1}. Optical visualization and SEM images of the pristine surfaces of the planar zinc and the PZEs can

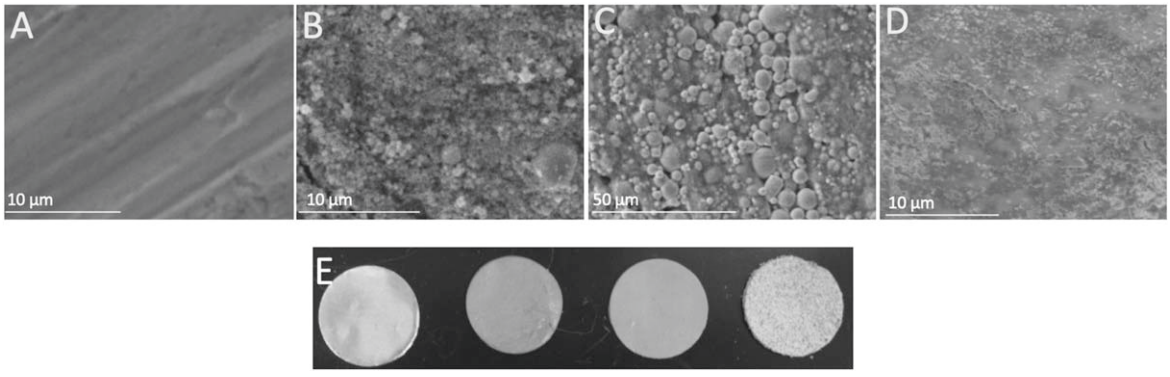

Figure 2. SEM images of the pristine planar and porous zinc anodes made from different zinc particle sizes (a)–(d). (a) planar zinc; (b) 60 nm; (c)10 μm; (d) 150 μm. Optical visualization of zinc anodes (e) from the left planer zinc, 60 nm, 10 μm, and 150 μm.

be seen in Fig. 2. It is clear that the surface of planar zinc is relatively flat and smooth with only a few minor defects. Furthermore, the crystal structure of the planar zinc is oriented linearly. Individual particles cannot be seen on the surface, confirming that the zinc is planar. In contrast, the surface of the small PZE is rough with a large variety of different particles made of zinc and zinc oxide. More spherical particles that cover the surface of the small PZE are smaller compared to the intermediate and large PZEs. EDS spot mapping (supporting information Fig. 3) of the small PZE shows a larger amount of zinc oxide on the surface of the anode compared to the EDS maps of the intermediate and large PZEs. This is because larger surface area of the small PZE tends to be oxidized more easily compared to the intermediate and large PZEs, which causes a higher zinc oxide to zinc ratio on the surface. In Fig. 2C, the intermediate PZE surface can be seen. The surface is smoother than the small PZE and the individual particles are bigger. Larger pores are also now visible when compared with the small PZE. The surface of the large PZE can be seen in Fig. 2D. The surface of the large PZE is smoother than the other two PZEs. We hypothesize that the smoothness of the of the surface contributes to the electrodes stability to mitigate dendritic growth. The surface of the large PZE has fewer individual particles than the small and intermediate PZE. This is attributed to the larger different starting particle sizes of the materials during the mortar and pestle process. The intermediate PZE has the lowest difference in starting particle size with both the zinc and zinc oxide being 10 μm. The 60 nm nanoparticle zinc was too small to be crushed during the electrode fabrication process, so it has the largest number of individual particles. The 150 μm zinc particles can be crushed easily during the process allowing for a smooth porous surface. An optical comparison of the different PZEs and planar zinc is shown in Fig. 2E. The small and intermediate PZE have a smooth velvety surface, while the texture of the large PZE looks more similar to a sandpaper.

To evaluate the electrochemical performance of the PZEs towards energy storage applications, we tested each of the PZE using a variety of electrochemical conditions and then compared the results to each other (Fig. 3). The galvanostatic cycling of symmetric cells of the PZEs at a current density of 1 $mAcm^{-2}$ are shown in Fig. 3A. Increasing the starting zinc particle size is found to increase the cycle life of the zinc symmetric cells. Large PZE can be seen to have the longest cycle life among all PZEs, showing stable cycling for 700 h. Cells made from the intermediate PZE last for around 450 h before failing. Both the intermediate and large PZEs outperform the planar zinc anodes. The voltage plateaus of the intermediate PZE are higher than the voltage plateaus of the large PZE. The galvanostatic cycling tests with higher current density of 2 mA cm^{-2} and 5 mA cm^{-2} were also performed and the results can be found in supporting information Fig. 4. The large PZE fails around 450 h for both tests while planar zinc fails at 275 h and 240 h respectively. The large PZE shows an increase into the voltage plateau as the applied current increases, while the planar zinc maintains the same plateau for all three currents applied. Small PZE preforms very poorly and fail with in the first ten cycles of the battery and are very unstable with a larger voltage plateau range from −1 V to 1 V. The large voltage spikes on the charge and discharge cycles disappear once the dendrite pierces the separator and creates an internal short in the cell, causing the voltage to go to zero. The poor performance of the small PZE is attributed to the increased amount of zinc oxide on the surface of the anode. Zinc oxide increases the affinity of water splitting and insulates active material on the electrode.[26] Since there is more zinc oxide on the surface of the electrode than zinc, the battery is more prone to large unstable voltage spikes and hydrogen evolution during the charge/discharge process. Further evidence of the increased amount of zinc oxide on the surface of the small PZE can be seen in the Nyquist plots in Fig. 3B. The interfacial resistance of the small PZE is larger than the interfacial resistance of the intermediate and large PZEs. The interfacial resistances of all three PZEs are much smaller than planar zinc, indicating less energy is required to strip and plate zinc ions on the PZEs. Due to the poor performance of the small PZE during initial testing, further electrochemical and characterization tests are focused on the intermediate and large PZE exclusively. In Fig. 3C, LSV results of the Zn || stainless steel cell can be seen. It is clear that zinc stripping and platting on the stainless-steel electrodes are visible at −0.2 V & 0.2 V for all PZEs as well as the planar zinc. Electrolyte decomposition occurs around 2.7 V for the large PZE, while it occurs around a slightly lower voltage of 2.6 V for planar zinc and intermediate PZE. In Fig. 3D, DoD_{zn} results are shown. Intermediate PZE has a DoD_{zn} of 41%, while the large PZE has a DoD_{zn} of 45%. DoD_{zn} of the Planar zinc is found to be 25%. The lower resistance and energy requirement to strip zinc ions from the PZEs allow for a higher depth of discharge to be achieved in these electrodes. The voltage profiles of the DoD_{zn} tests can be found in Supporting information Fig. 5. The intermediate PZE has a capacity of 89 mAh while the large PZE has a capacity of 57 mAh. The planar zinc has a capacity of 21 mAh. The DoD_{zn} was found by multiplying the weight of each anode with the theoretical capacity of zinc. The batteries were then discharged till failure and then the actual capacity was compared to the theoretical capacity.

Previous research has reported that planar zinc electrode, during plating and stripping cycles, prefers to deposit in the (002) plane as a hexagonal close packed (HCP) crystal structure.[27–29] Our results agree with these findings and can be seen in Fig. 4 which shows SEM images of different cycled zinc electrodes. By viewing the cycled batteries, we can observe the changes to the surface morphology of the zinc in order to determine which features improve cycle stability. In Fig. 4A, HCP zinc crystal deposits can be seen on the surface of the planar zinc electrode. Compared to the smooth surface of planar zinc at the pristine state seen in Fig. 1, over many cycles, the surface of the planar zinc is covered with plated zinc crystals. The crystal structure of the deposited zinc is HCP which is the preferred zinc morphology during electrodeposition. Due to the kinetic instability that occurs when currents above the DLC are used during the plating and stripping cycles, these crystals do not plate parallel to the surface. Instead, the zinc HCP deposits stack unevenly on top of each other creating areas with higher local currents. This causes more uneven plating to occur and begins the dendritic cycle, which eventually results in internal shorted induced battery failure. Figure 4B shows SEM images of a cycled small PZE after short circuit. The deposits on the small PZE are similar to the deposits found planar zinc with an HCP crystal structures. However, the deposits on the intermediate and large PZE indicates a shift from HCP crystal deposits to amorphous zinc metal deposits as the zinc particle size increases. Furthermore, the surface of the small PZE is covered with these HCP crystals during the first few cycles of galvanostatic cycling as seen in Fig. 3A when the small PZE fails before reaching 10 cycles. This indicated that the small PZE is worse for the mitigation of dendrites compared to the intermediate and large PZEs. In Fig. 4C, SEM images of cycled intermediate PZE show an increased affinity to deposit in the separator compared to the rest of the PZE and planar zinc. The intermediate zinc has the highest affinity to deposit on the glass microfiber separator, which we believe is caused by the similar size of the zinc relative to the pores of the glass microfiber separator used. Previous studies show similar effect on the planar zinc electrode that zinc tends to deposit the glass microfiber due to its ability to regulate ion transport behavior.[30,31] While the glass fiber smooths the zinc deposition of the intermediate PZE, the zinc deposited in the separator decrease the amount of active zinc material inside the electrode, therefore, decreasing the performance of the cell over continuous cycling. In Fig. 4D, SEM images of large PZE show uniform and smooth plating compared to the HCP crystals seen on planar and small PZE. The zinc deposits on the surface of the large PZE is amorphous zinc metal. We believe that these amorphous deposits are the main reason for the increased stability and overall performance of the cell.

To evaluate the morphological evolution of the intermediate and large PZEs at various cycles, we examined the SEM images of intermediate and large PZEs to see how the surface changed over

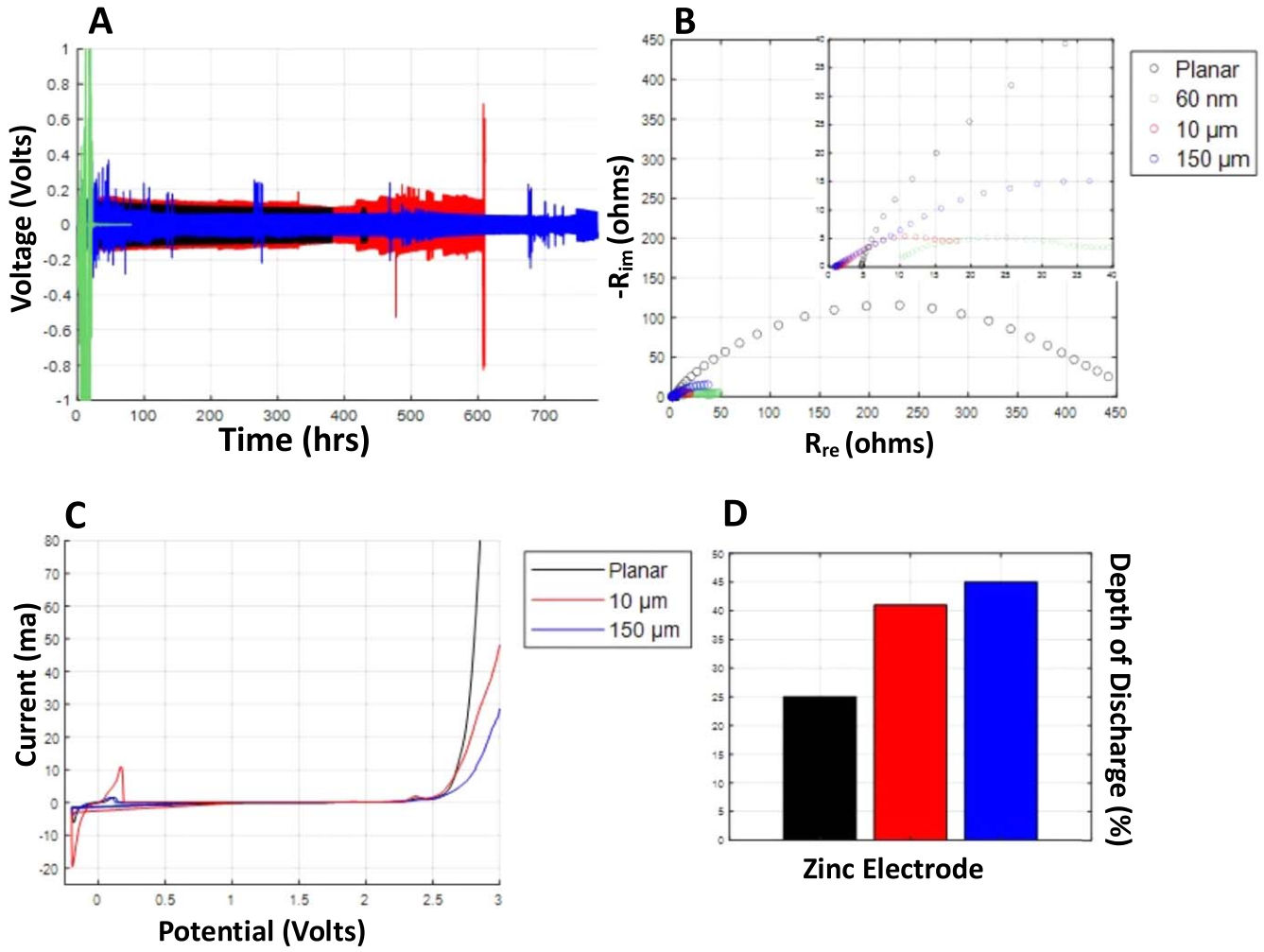

Figure 3. Electrochemical characterization of the PZEs fabricated from different starting particle sizes. (a) Galvanostatic cycling of symmetric coin cells of various starting particle sizes. All tests occur under a current density of 1 mA cm^{-2} and use a electrolyte of 2 M $ZnSO_4$ + 5 wt% PEG300. (b) EIS Nyquist plot comparing the resistance of different porous anodes to planar zinc. Insect shows a zoomed in scale of (b). (c) LVS curves comparing 150 *u*m PZE, 10 *u*m PZE and planar zinc at a scan rate of 1 mV s^{-1}. (d) Depth of discharge testing comparing 150 *u*m PZE, 10 *u*m PZE and planar zinc.

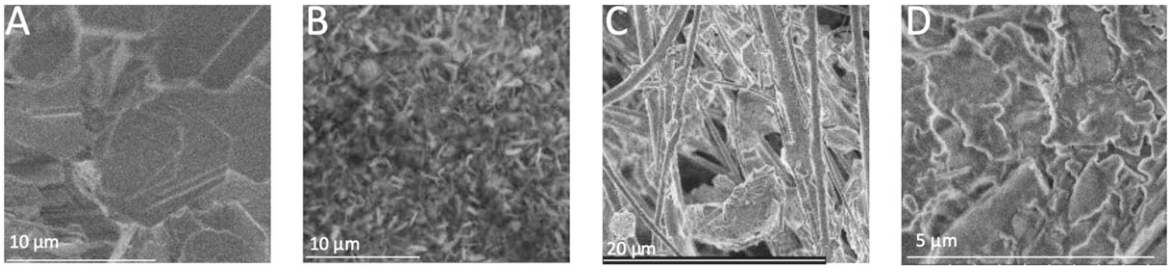

Figure 4. SEM images of zinc electrodes made from different particle sizes. Symmetric coin cells in an electrolyte of 2 M ZnSO4 + 5 wt% PEG300 are tested under a constant current of 1 $mAcm^{-2}$ until failure. (a) planar zinc (b) 60 nm (c)10 μm (d) 150 μm.

time and the results can be found in Fig. 5. SEM images of intermediate PZEs at 10, 20, and 100 cycles respectively can be seen in Figs. 5A–5C. Very littles changes can be observed from the pristine surface of the intermediate PZE compared to the surface at 10 cycles. After 20 cycles, small deposits of amorphous zinc can be seen. After cycling the intermediate PZE for 100 cycles, the surface has changed from the rough, bumpy surface to a smoother surface covered by zinc deposits. Large zinc deposits bound to the glass fiber separator can also be seen. Figures 5D–5F show SEM images of large PZE at 10, 20, and 100 cycles respectively. Similarly, to the intermediate PZE, not many changes in morphology can be found on the surface of the large PZE after 10 cycles. After 20 cycles, the surface is still similar to the pristine surface of the large PZE. After 100 cycles, amorphous zinc deposits can be seen on the surface, while most of the amorphous zinc are deposited on the large PZE electrode surface instead of on the glass fiber separator.

To confirm the crystal structure of the deposited zinc at different electrode surfaces, we preformed XRD analysis on planar zinc, intermediate and large PZEs. The results can be found in Fig. 6. The XRD patterns of the PZE are similar regardless of the starting particle size. From the XRD analysis of the intermediate PZE, it is confirmed that the deposit structure changes from HCP crystals to

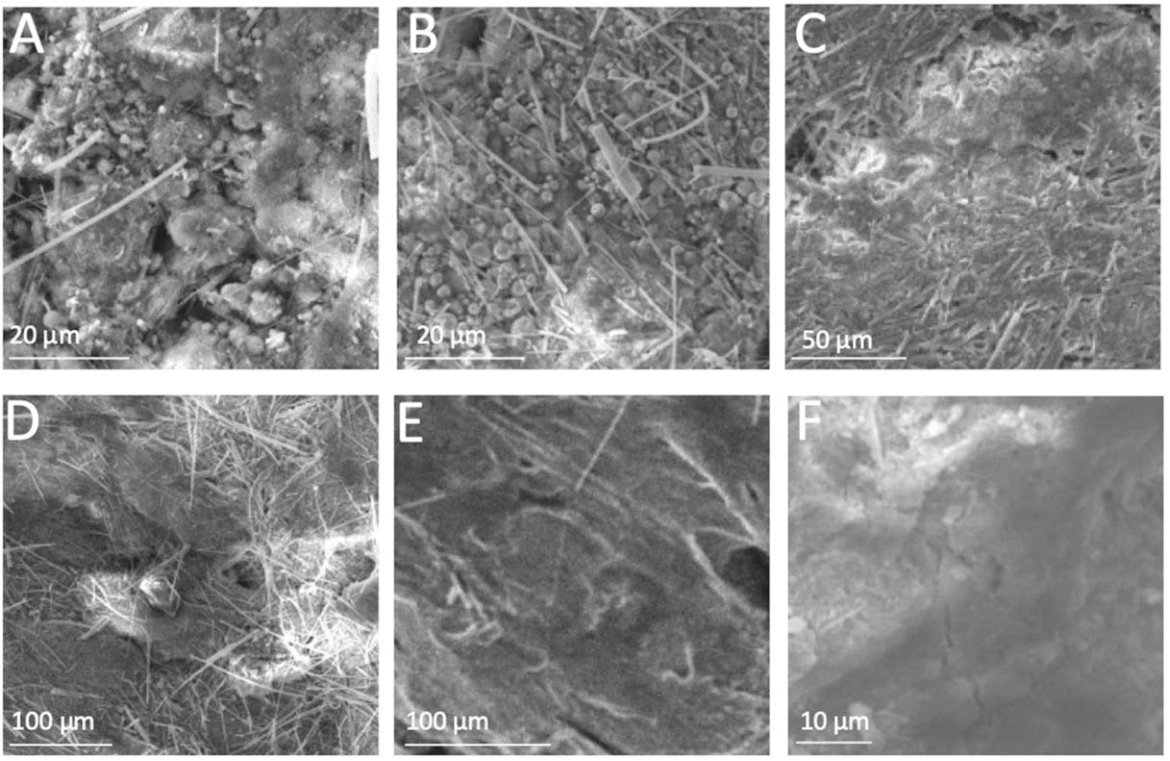

Figure 5. Intermediate and large PZE from various cycles to view surface changes over time. on the top row is intermediate PZE at (a)10 cycle, (b) 20 cycles, (c) 100 cycles while the bottom row is large PZE at (d)10 cycle, (e) 20 cycles, (f) 100 cycles

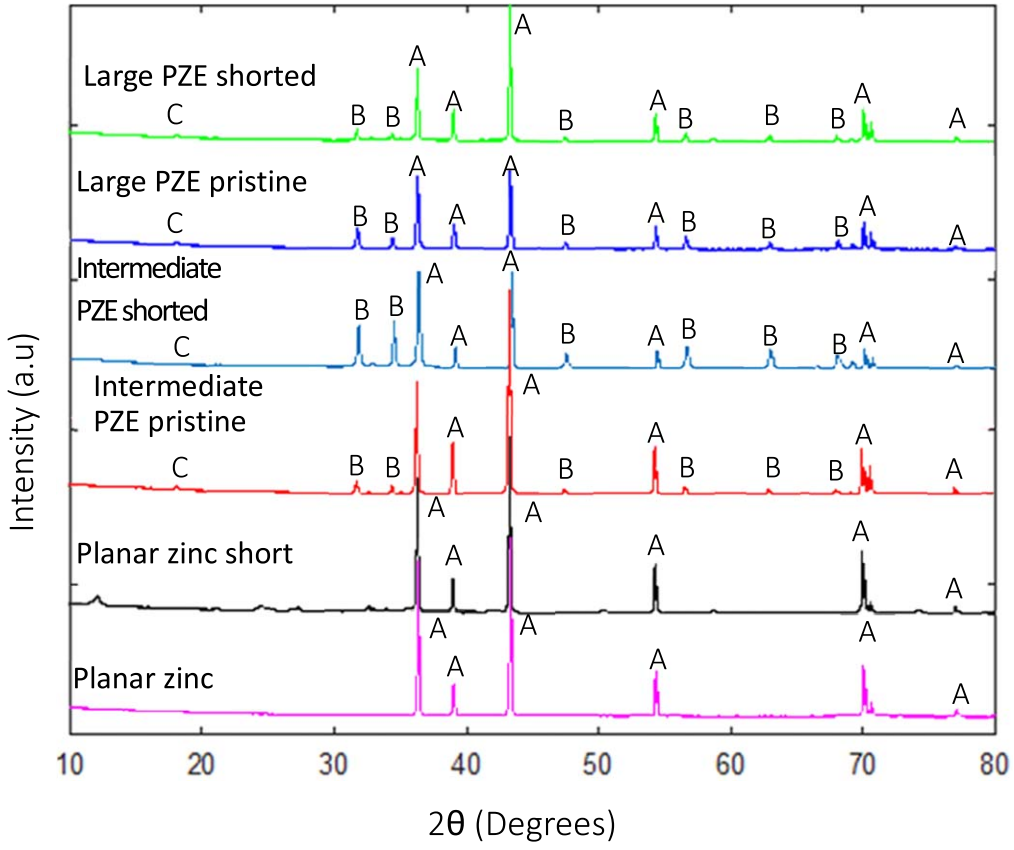

Figure 6. XRD analysis of pristine and cycled anodes. Peaks for A: Zinc (98-000-0482), B: Zinc Oxide (98-000-0483), and C: PTFE (00-047-2217) are shown.

amorphous zinc as the size of the zinc particles increase from the nanoscale to the microscale. XRD results of the small PZE can be

found in Supporting information Fig. 6. Full width half mass (FWHM) values can be found in Supporting information Table II, which follows the correlation between microparticle size and FWHM described by the Scherrer equation. Furthermore, the cycled intermediate PZE had a zinc-to-zinc oxide ratio of almost 3 to 1 while the pristine intermediate PZE had a ratio of nearly 4 to 1. The pristine large PZE had a starting zinc-to-zinc oxide ratio of nearly 2 to 1. After cycling the large PZE until failure, the zinc-to-zinc oxide ratio became 3 to 2. This suggests that the zinc oxide passivation layer evolves differently in the intermediate and large PZEs. We believe the different ratios of zinc-to-zinc oxide in the pristine anodes is caused by the intermediate zinc particles being the same size as the ZnO particles while the large zinc particles are much larger. The higher zinc-to-zinc oxide ratio of the intermediate PZE compared to the large PZE might explain the larger voltage plateaus that can be seen in Fig. 3A. the higher zinc-to-zinc oxide ratio leads to more surface passivation during the cycling causing the voltage to increase until the voltage reached the safety limit set on the tester. The shorted planar zinc anode did not show the same zinc oxide peaks as the intermediate and large PZEs. We believe this is due to zinc oxide depositing as an amorphous structure or the crystal size being too small to be detected by the XRD instrucment.[32] Zinc oxide peaks can be seen on both the intermediate and large PZE. The peak intensity of the ZnO decreases from the pristine large PZE to the cycled one indicating that it gets reduced to zinc during cycling. The opposite effect is seen on the intermediate PZE where the peak intensity of ZnO increases from the pristine anode to the shorted one. This agrees with our failure mechanism during galvanostatic cycling that the zinc oxide increases the resistance of the cell until its eventual failure. The failure is also accredited to the loss of active material being deposited onto the glass microfibers instead of the counter electrode, which can be seen in the SEM images of the intermediate PZE is as little as 10 cycles. The Large PZE anode shows a decrease in peak intensity at 36° which corresponds to the (002) HCP crystal structure. This agrees with our prior findings that zinc does not deposit as HCP crystals, but as amorphous zinc on the large PZE. Furthermore, the intensity of the (002) peak is much higher in the planar zinc than in either the intermediate or large PZE. The peak corresponding to the (101) crystal structure at 43° increases in intensity in both PZEs and the planar zinc sample. We believe this is caused by the uneven dendritic growth during the galvanostatic plating and stripping cycles. When comparing the intensities of the (002) and (101) peaks between the pristine and cycled anodes (Supporting information Table I), we found that the ratio between the two peaks decreases for the large PZE while it increases for the intimidate PZE. The ratio of the (002) peak to the (101) peak in the planar zinc does not change very much. The peak at 18° is found to be PTFE. The peak intensity was consistent in the pristine and cycled anodes.

Conclusions

In summary, PZE made from large zinc particles has been shown to outperform PZEs made from small and intermediate particle sizes. Larger PZE are better suited to limit dendrite growth due to their ability to promote even plating. SEM and XRD of the cycled PZEs show that zinc deposits as amorphous instead of the HCP structure seen in planar zinc. The increased surface area of the anode also lowers the local diffusion limiting current, allowing for over 700 h of striping and plating at a current of 1mAcm^{-2}. However, the life span of the planar zinc span is less than half of the total life span of the large PZE. The incorporation of zinc oxide throughout the electrode is found to mitigate the formation of a passivation layer on the surface of the anode and improve electrolyte stability in the large PZE as well. The electrolyte in the planar zinc cell started to decompose at 2.6 V while it decomposes at 2.7 V in the large PZE cell. Large PZE electrodes show promise as a potential anode candidate for zinc-air batteries. However, the performance of the anode still needs to be improved further in order for the PZE to compete with LiBs. One potential research pathway to further improve these PZEs is to investigate the effects of the addition of dopants inside the starting zinc particles.

Acknowledgments

This work was supported by the National Science Foundation Award Number 2119688. S.W. also acknowledges the financial support from the University of New Mexico startup fund.

ORCID

Shuya Wei https://orcid.org/0000-0001-9269-1950

References

1. L. Xie, C. Tang, Z. Bi, M. Song, Y. Fan, C. Yan, X. Li, F. Su, Q. Zhang, and C. Chen, "Hard carbon anodes for next-generation Li-Ion batteries: review and perspective." *Adv. Energy Mater.*, **11**, 2101650 (2021).
2. M. Winter, B. Barnett, and K. Xu, "Before Li Ion Batteries." *Chem. Rev.*, **118**, 11433 (2018).
3. Y. Wang, E. Sahadeo, G. Rubloff, C.-F. Lin, and S. B. Lee, "High-capacity lithium sulfur battery and beyond: a review of metal anode protection layers and perspective of solid-state electrolytes." *J. Mater. Sci.*, **54**, 3671 (2019).
4. C. Wang, Y. Yu, J. Niu, Y. Liu, D. Bridges, X. Liu, J. Pooran, Y. Zhang, and A. Hu, "Recent progress of metal–air batteries—a mini review." *Applied Sciences*, **9**, 2787 (2019).
5. C. Li, X. Xie, S. Liang, and J. Zhou, "Issues and future perspective on zinc metal anode for rechargeable aqueous zinc-ion batteries." *Energy & Environmental Materials*, **3**, 146 (2020).
6. L. E. Blanc, D. Kundu, and L. F. Nazar, "Scientific challenges for the implementation of Zn-ion batteries." *Joule*, **4**, 771 (2020).
7. L. Cao et al., "Fluorinated interphase enables reversible aqueous zinc battery chemistries." *Nat. Nanotechnol.*, **16**, 902 (2021).
8. R. Yuksel, O. Buyukcakir, W. K. Seong, and R. S. Ruoff, "Metal-organic framework integrated anodes for aqueous zinc-ion batteries." *Adv. Energy Mater.*, **10**, 1904215 (2020).
9. F. Wang, O. Borodin, T. Gao, X. Fan, W. Sun, F. Han, A. Faraone, J. A. Dura, K. Xu, and C. Wang, "Highly reversible zinc metal anode for aqueous batteries." *Nat. Mater.*, **17**, 543 (2018).
10. D. Lin, Y. Liu, and Y. Cui, "Reviving the lithium metal anode for high-energy batteries." *Nat. Nanotechnol.*, **12**, 194 (2017).
11. M. B. Lim, T. N. Lambert, and B. R. Chalamala, "Rechargeable alkaline zinc–manganese oxide batteries for grid storage: Mechanisms, challenges and developments." *Materials Science and Engineering: R: Reports*, **143**, 100593 (2021).
12. V. Verma, S. Kumar, W. Manalastas, and M. Srinivasan, "Undesired reactions in aqueous rechargeable Zinc Ion batteries." *ACS Energy Lett.*, **6**, 1773 (2021).
13. Y. Ito, M. Nyce, R. Plivelich, M. Klein, and S. Banerjee, "Gas evolution in a flow-assisted zinc–nickel oxide battery." *J. Power Sources*, **196**, 6583 (2011).
14. D. Zhang, A. J. Warren, G. Li, Z. Cheng, X. Han, Q. Zhao, X. Liu, Y. Deng, and L. A. Archer, "Electrodeposition of zinc in aqueous electrolytes containing high molecular weight polymers." *Macromolecules*, **53**, 2694 (2020).
15. P. Lin, J. Cong, J. Li, M. Zhang, P. Lai, J. Zeng, Y. Yang, and J. Zhao, "Achieving ultra-long lifespan Zn metal anodes by manipulating desolvation effect and Zn deposition orientation in a multiple cross-linked hydrogel electrolyte." *Energy Storage Mater.*, **49**, 172 (2022).
16. D. E. Turney et al., "Rechargeable zinc alkaline anodes for long-cycle energy storage." *Chem. Mater.*, **29**, 4819 (2017).
17. H. He, H. Tong, X. Song, X. Song, and J. Liu, "Highly stable Zn metal anodes enabled by atomic layer deposited Al2O3 coating for aqueous zinc-ion batteries." *J. Mater. Chem. A*, **8**, 7836 (2020).
18. D. Lee, H.-I. Kim, W.-Y. Kim, S.-K. Cho, K. Baek, K. Jeong, D. B. Ahn, S. Park, S. J. Kang, and S.-Y. Lee, "Water-repellent ionic liquid skinny gels customized for aqueous Zn-Ion battery anodes." *Adv. Funct. Mater.*, **31**, 2103850 (2021).
19. Y. Tian, Y. An, Y. Yang, and B. Xu, "Robust nitrogen/selenium engineered MXene/ZnSe hierarchical multifunctional interfaces for dendrite-free zinc-metal batteries." *Energy Storage Mater.*, **49**, 122 (2022).
20. Z. Yuan, X. Liu, W. Xu, Y. Duan, H. Zhang, and X. Li, "Negatively charged nanoporous membrane for a dendrite-free alkaline zinc-based flow battery with long cycle life." *Nat. Commun.*, **9**, 3731 (2018).
21. M. Chamoun, B. J. Hertzberg, T. Gupta, D. Davies, S. Bhadra, B. Van Tassell, C. Erdonmez, and D. A. Steingart, "Hyper-dendritic nanoporous zinc foam anodes." *NPG Asia Mater.*, **7**, e178 (2015).
22. W. Sun et al., "Zn/MnO2 battery chemistry With H + and Zn2 + Coinsertion." *JACS*, **139**, 9775 (2017).
23. C. W. Lee, K. Sathiyanarayanan, S. W. Eom, H. S. Kim, and M. S. Yun, "Novel electrochemical behavior of zinc anodes in zinc/air batteries in the presence of additives." *J. Power Sources*, **159**, 1474 (2006).
24. Y. Xu, Y. Zhang, Z. Guo, J. Ren, Y. Wang, and H. Peng, "Flexible, stretchable, and rechargeable fiber-shaped zinc–air battery based on cross-stacked carbon nanotube sheets." *Angew. Chem. Int. Ed.*, **54**, 15390 (2015).
25. J. Duay, T. N. Lambert, M. Kelly, and I. Pineda-Dominguez, "Rechargeable solid-state copper sulfide cathodes for alkaline batteries: importance of the copper valence state." *J. Electrochem. Soc.*, **166**, A687 (2019).

26. R. W. Powers and M. W. Breiter, "The anodic dissolution and passivation of Zinc in concentrated potassium hydroxide solutions." *J. Electrochem. Soc.*, **116**, 719 (1969).
27. H. Liu, Y. Zhang, C. Wang, J. N. Glazer, Z. Shan, and N. Liu, "Understanding and controlling the nucleation and growth of Zn electrodeposits for aqueous zinc-ion batteries." *ACS Appl. Mater. Interfaces*, **13**, 32930 (2021).
28. S. Jin et al., "Stabilizing Zinc electrodeposition in a battery anode by controlling crystal growth." *Small*, **17**, 2101798 (2021).
29. W. Sun et al., "A rechargeable zinc-air battery based on zinc peroxide chemistry." *Science*, **371**, 46 (2021).
30. J. Ming, J. Guo, C. Xia, W. Wang, and H. N. Alshareef, "Zinc-ion batteries: Materials, mechanisms, and applications." *Materials Science and Engineering: R: Reports*, **135**, 58 (2019).
31. W. Du, E. H. Ang, Y. Yang, Y. Zhang, M. Ye, and C. C. Li, "Challenges in the material and structural design of zinc anode towards high-performance aqueous zinc-ion batteries." *Energy Environ. Sci.*, **13**, 3330 (2020).
32. M. B. Lim, T. N. Lambert, and E. I. Ruiz, "Effect of ZnO-saturated electrolyte on rechargeable alkaline zinc batteries at increased depth-of-discharge." *J. Electrochem. Soc.*, **167**, 060508 (2020).